

Quantifying Tumor Microvasculature With Optical Coherence Angiography and Intravoxel Incoherent Motion Diffusion MRI

W. Jeffrey Zabel¹, Héctor Contreras-Sánchez², Warren Foltz³, Costel Flueraru⁴, Edward Taylor⁵, and Alex Vitkin⁶

Abstract—Intravoxel Incoherent Motion (IVIM) MRI is a contrast-agent-free microvascular imaging method finding increasing use in biomedicine. However, there is uncertainty in the ability of IVIM-MRI to quantify tissue microvasculature given MRI’s limited spatial resolution (mm scale). Nine NRG mice were subcutaneously inoculated with human pancreatic cancer BxPC-3 cells transfected with DsRed, and MR-compatible plastic window chambers were surgically installed in the dorsal skinfold. Mice were imaged with speckle variance optical coherence tomography (OCT) and colour Doppler OCT, providing high resolution 3D measurements of the vascular volume density (VVD) and average Doppler phase shift ($\overline{\Delta\phi}$) respectively. IVIM imaging was performed on a 7T preclinical MRI scanner, to generate maps of the perfusion fraction f , the extravascular diffusion coefficient D_{slow} , and the intravascular diffusion coefficient D_{fast} . The IVIM parameter maps were coregistered with the optical datasets to enable direct spatial correlation. A significant positive correlation was noted between OCT’s VVD and MR’s f (Pearson correlation coefficient $r = 0.34, p < 0.0001$). Surprisingly, no significant correlation was found between $\overline{\Delta\phi}$ and D_{fast} . This may be due to larger errors in the determined D_{fast} values compared to f , as

confirmed by Monte Carlo simulations. Several other inter- and intra-modality correlations were also quantified. Direct same-animal correlation of clinically applicable IVIM imaging with preclinical OCT microvascular imaging support the biomedical relevance of IVIM-MRI metrics, for example through f ’s relationship to the VVD.

Index Terms—IVIM-MRI, OCT angiography, tumour microvasculature, multimodal imaging, microvascular imaging.

I. INTRODUCTION

THE structure and function of the tumour microvascular network plays a crucial role in determining cancer therapy treatment outcome. Compared to healthy tissue, the microvasculature in tumours is highly disorganized and tortuous with closed ends, shunts, and avascular regions. This disorganized network leads to the formation of radiation resistant hypoxic regions [1] and makes it difficult to deliver intravenous cancer therapies like chemotherapy since these therapeutics cannot be uniformly delivered to the cancer cells [2].

There are several new therapies that specifically target the microvascular network with the goal of ‘normalizing’ it by administration of vascular targeting agents such as VEGF blockades [3]. These agents act to prune the vascular network and induce a more normal state that reduces hypoxia and increases blood flow and nutrient delivery to the surrounding cells thus making treatments during this state more effective [4]. Evidence also suggests that the high dose per fraction delivered during stereotactic body radiation therapy induces vascular ablation which could be an important determinant of tumour treatment response [5].

Given the importance of the microvascular network in determining treatment response and the development of vascular targeting agents that aim to modify it, there is growing interest in non-invasively characterizing tissue microvasculature in the clinic. Quantification of the structure and function of the microvascular network may enable treatment personalization by selectively targeting radiation therapy to hypoxic regions of the tumour (‘dose painting’) [6] or by modifying the fractionation schedule based on the perfusion/hypoxic level

Received 16 April 2025; revised 10 August 2025; accepted 4 September 2025. Date of publication 10 September 2025; date of current version 4 February 2026. This work was supported in part by the Canadian Institutes of Health Research under Grant 202010PJT-451556-MPI-ADHD-40858, in part by the Ontario Graduate Scholarship, in part by the STARS21 Program, and in part by the Princess Margaret Cancer Foundation. Recommended by Associate Editor A. Frangi. (Corresponding author: W. Jeffrey Zabel.)

This work involved human subjects or animals in its research. Approval of all ethical and experimental procedures and protocols was granted by the University Health Network’s Institutional Animal Care and Use Committee in Toronto, Canada.

W. Jeffrey Zabel is with the Department of Radiation Oncology, Stanford University School of Medicine, Palo Alto, CA 94304 USA (e-mail: wjzabel@stanford.edu).

Héctor Contreras-Sánchez and Alex Vitkin are with the Department of Medical Biophysics, University of Toronto, Toronto, ON M5G 2C4, Canada (e-mail: hectoralex.contreras@mail.utoronto.ca; Alex.Vitkin@uhn.ca).

Warren Foltz is with the Department of Radiation Oncology, University of Toronto, Toronto, ON M5T 1P5, Canada (e-mail: Warren.Foltz@uhn.ca).

Costel Flueraru is with the Quantum and Nanotechnologies Research Centre, National Research Council of Canada, Ottawa, ON K1A 0R6, Canada (e-mail: Costel.Flueraru@nrc-cnrc.gc.ca).

Edward Taylor is with the Department of Physics, Toronto Metropolitan University, Toronto, ON M5B 1E9, Canada (e-mail: edward.taylor@torontomu.ca).

Digital Object Identifier 10.1109/TMI.2025.3607752

of the tumour to allow for reoxygenation [7]. Microvascular quantification would also allow for the monitoring of the action of vascular targeting agents to determine when the vasculature has been sufficiently normalized to inform the timing of treatment delivery [4].

Common clinical imaging modalities such as CT and MRI are useful in cancer therapy since they can image to any depth into the tissue however they lack the necessary spatial resolution (mm scale) to directly visualize the microvascular network (μm scale). Therefore, perfusion CT and MRI techniques rely on pharmacokinetic models applied to concentration-time curves to extract microvascular information beyond the imaging resolution of the scanner [8]. For example, in dynamic contrast enhanced (DCE) MRI, the gadolinium-based contrast agent diffusion coefficient from the intravascular to the extravascular space, k_{trans} , has shown good potential in monitoring the action of vascular targeting drugs [9] and predicting radiotherapy treatment outcomes [10]. However, DCE-CT and MRI are not suitable for repeat imaging due to the use of ionizing radiation (in the case of CT) and the risk of gadolinium deposition [11]. Furthermore, the need for precise timing and dose of the contrast agent during the scan and documented reproducibility uncertainties [12] complicates the procedure and makes it difficult to standardize.

Intravoxel Incoherent Motion (IVIM) MRI is a non-contrast-enhanced perfusion imaging method [13] that is being used more often in oncology and beyond [14]. IVIM is based on the principle of diffusion weighted imaging (DWI) where multiple strengths of diffusion-encoding gradients (b-values) are used to assess the signal decay resulting from the motion of water molecules within the tissue between gradient pulses. At b-values above 200 s/mm^2 , the signal attenuation is dominated by the ‘slow’ water diffusion in the extravascular space. However, at b-values less than 200 s/mm^2 , faster processes can be quantified. Flowing blood in the microvasculature acts as a pseudo-diffusion process which can be measured by analyzing the signal decay at these small b-values [15]. The biexponential IVIM model (which includes slow ‘extravascular’ and fast ‘intravascular’ diffusion exponential decay terms) can be fitted to the signal attenuation vs. b-value image sets on a voxel-by-voxel basis to extract the extravascular diffusion coefficient D_{slow} and the intravascular diffusion coefficient D_{fast} . In the limit where blood flows through many segments during the interval between gradient pulses, the average blood speed \bar{v} is related to D_{fast} by the relationship $D_{fast} = l\bar{v}/6$ where l is the average vessel segment length [15]. The fractional flowing blood volume f is another metric that can be calculated from the biexponential fit to the data. Thus f and D_{fast} may be two useful perfusion parameters for quantifying the structure and function of the microvasculature, as they are theoretically correlated with the tissue vascular volume density and mean blood speed respectively.

Despite the potential benefits of using IVIM in the clinic, it must first be validated against standard measurements of the microvascular network, including the vascular volume density and mean blood velocity [15]. To this end, some studies correlated microvessel density assessed with histology with f [16], [17], however histology suffers from being a 2D

ex-vivo analysis of a 3D vascular network and blood speed cannot be assessed. Other studies correlate IVIM parameters with different types of contrast agent-based perfusion MRI showing good correlations [18], [19]; however, other studies have not seen these linkages [20], [21]. Correlating IVIM with other perfusion MRI techniques is an indirect measure of the microvasculature and suffers from its own quantification uncertainties [22]. A comprehensive review of these studies can be found in [23].

Intravital microscopy in window chamber preparation mouse tumour models [24], [25], [26], [27] presents a promising new technique for perfusion MRI validation. In previous work, we designed and 3D printed an MR compatible plastic window chamber and developed a coregistration software for direct spatial correlation analysis between perfusion MRI and high-resolution optical images [27]. Specifically, we used speckle variance optical coherence tomography (svOCT) as our ‘ground truth’ microvascular imaging modality [28]. The microvascular imaging capabilities of svOCT has been previously validated using confocal fluorescence microscopy with intravenously injected Fluorescein-labelled Dextran [29]. svOCT, has distinct advantages over other intravital microscopy techniques because it does not require contrast agents and can image over a large field of view in 3D to a depth of $\sim 2 \text{ mm}$, which enables improved 3D coregistration with MRI (compared to, for example, the shallow depth and small FOV’s in confocal intravital microscopy imaging of the microvasculature [24], [25]). We previously evaluated this platform by correlating DCE-MRI with svOCT images of the microvasculature and found that DCE-MRI metrics such as the time to peak contrast enhancement correlated well with microvascular density [26].

Given the recent rise in use of IVIM in oncology [14], the simplicity of contrast-agent-free clinical imaging, and the need to establish its microvascular imaging capabilities *in-vivo* [15], [22], we thus extend and expand our previous work [26], [27] to assess IVIM-MRI. Here we will directly correlate ground truth measurements of microvessel density (obtained with svOCT) with IVIM measurements of f . To directly assess the ability of D_{fast} to measure blood flow, we have also employed colour Doppler OCT (DOCT) imaging to provide ground truth measurements of blood flow [30]. This work will give a better understanding of the ability of IVIM to quantify microvascular structure and function towards its use in the clinic for non-invasive microvascular quantification for treatment monitoring and personalization.

II. METHODS

A. Animal Preparation

$n = 9$ female NOD-Rag1^{null} IL2rg^{null} (NRG) immunocompromised mice were subcutaneously inoculated with human pancreatic cancer cells (BxPC-3) transfected with DsRed for viability assessment [31]. When tumours grew to a diameter of $\sim 3\text{-}5 \text{ mm}$ (typically 24-28 days post inoculation), 3D printed biocompatible plastic window chambers were surgically sutured to the dorsal skin folds (Fig 1AB) as described in [27]. Inoculation, surgery, and imaging were all

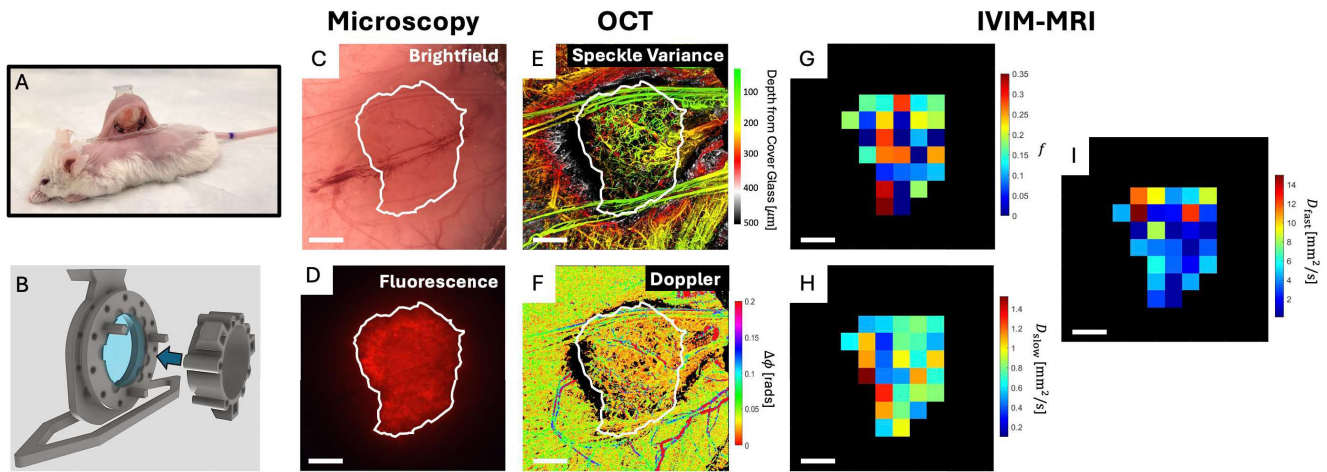


Fig. 1. Animal model, optical, and MR imaging. (A) Dorsal skinfold window chamber mouse model with human pancreatic cancer xenograph. (B) Custom designed 3D printed plastic window chamber enables both optical and MR imaging, a fiducial marker ring can be affixed to coregister the optical and MRI datasets. (C) Brightfield, and (D) fluorescence microscopy. (E) Depth encoded svOCT microvascular image provides the structure of the microvascular network. (F) DOCT imaging provides the Doppler phase shift $\Delta\phi$ [radians], which is related to average axial blood flow speed. (G-I) IVIM-MRI parametric images from fits to (1). (G) Perfusion fraction f [range between 0 and 1]. (H) Extravascular diffusion coefficient D_{slow} [mm^2/s]. (I) Intravascular diffusion coefficient D_{fast} [mm^2/s]. C-I are coregistered. Solid white line in C-F is the tumour boundary; IVIM parameters are only shown for voxels within the tumour contour (G-I). Scale bar = 1 mm. (A) is reprinted from [27] with permission.

performed with the mice under general anesthesia (5% isoflurane for induction, 2% for maintenance, 0.5 L/min oxygen flow rate).

B. Optical Imaging: Experimental Setup

All optical and MR imaging was performed on the same day two weeks post DSWC surgery to allow for maturation of the tumour microvascular network and animal recovery from surgery. Mice were anesthetised and secured to a warmed stage for body temperature regulation. Brightfield (Fig. 1C) and DsRed fluorescence (Fig. 1D) imaging was performed for tumour localization and viability assessment, using an epifluorescence microscope (Leica Microsystems MZ FLIII, Richmond Hill, ON, CA) with consistent exposure times.

Depth-resolved OCT images were acquired on a previously described swept source OCT system with a 1,310 nm centre wavelength and 110 nm bandwidth [32]. The axial and lateral resolutions in air for this system were $8 \mu\text{m}$ and $15 \mu\text{m}$ respectively. For svOCT, 24 axial scans (B-scans) were acquired per location over a $6 \times 6 \text{ mm}^2$ field of view to enable inter-frame speckle intensity variance calculations (Fig. 1E) [28]. Phase-resolved DOCT was used to measure the Doppler phase shift caused by the motion of red blood cells ($\Delta\phi$, Fig. 1F). 3D scans within the same field of view were acquired using an A-scan density of 4,000 A-scans/mm. The motion sensitivity of DOCT in our system for such scanning configuration was determined by the full width at half maximum (FWHM) of a static tissue-like phantom and found to be 32 mrad [30]. A high-pass frequency filter was applied prior to phase shift calculations for static tissue signal removal and fluid signal enhancement as described by Tang et al. [33]. The obtained metric $\Delta\phi$ thus provides quantitative axial blood flow velocity information. Only absolute magnitudes were considered for MRI-OCT correlations.

C. Optical Imaging: Data Analysis

For svOCT images, the vascular volume density (VVD) [fraction from 0-1] was calculated in the tumour region as defined by the DsRed fluorescence image. Segmentation was done up to a depth of $500 \mu\text{m}$ below the glass coverslip to restrict the analysis to the highest SNR region in the svOCT dataset. Vascular segmentation was performed in this region using a multi-step segmentation algorithm. Briefly, for each *en-face* (C-mode) scan, the following steps were applied sequentially: low pass Gaussian filter to reduce background noise, contrast enhancement using a top hat filter, and median filtering to reduce ‘salt and pepper’ speckle noise [34], [35]. Next, a step-down exponential filter was applied in the axial direction to reduce ‘streaking artifacts’ caused by the forward scattering of photons from red blood cells [35]. Finally, Otsu’s thresholding was applied to each C-scan [36]. Vessel segmentation accuracy was manually verified and corrected if segmentation errors were identified. To calculate the microvascular density of specific vessel diameters, a 3D morphological opening operation was performed using a spherical structuring element [37]. To remove noise from the DOCT phase shift data, the DOCT dataset was combined with the segmented svOCT vascular dataset and all non-vessel DOCT signals were set to zero.

To use DsRed fluorescence intensity as a measure of viable cellular density, only the signal from non-vessel regions must be considered since large vessels can decrease the signal despite the presence of dense cellular regions [38]. The sum of the DsRed fluorescence intensity was thus divided by the avascular volume, the latter calculated via $1 - \text{VVD}$.

D. MRI: Experimental Setup

MR imaging used a preclinical system (70/30 Biospec, Bruker Corporation, Ettlingen, DE), instrumented with the B-GAS-12 gradient coil insert, and 86 mm inner diameter

quadrature volume coil. Mice were anesthetised and placed in prone position on a dedicated murine scan table, including in-laid tubes connected to a circulating hot water heater for body temperature regulation. A MR-compatible physiologic monitoring system enabled respiratory monitoring (Model 1030; SA Instruments, Stony Brook, NY). A fiducial marker ring was affixed to the window chamber to enable coregistration of optical and MRI datasets (Fig 1B). The window chamber was secured in a 3D printed immobilization device to minimize motion [27]. A sagittal T2 weighed image set (TE = 25 ms; TR = 2,500 ms; 32 × 32 mm field-of-view with 128 × 128 matrix for 0.25 × 0.25 mm in-plane resolution; at least 11 imaging slices; 0.5 mm slice thickness) was iteratively reoriented until it aligned with the tumour and fiducial markers in the plane of the DSWC. Once the image set was aligned, IVIM diffusion weighted imaging was performed using 3 averages (TE = 16 ms; TR = 800 ms; 32 × 32 mm field of view with 64 × 64 matrix for 0.5 × 0.5 mm in-plane resolution; 0.5 mm slice thickness; gradient duration = 2.2 ms; gradient separation = 9 ms; total scan time = 61 minutes) with the following b-values: 0, 20, 40, 60, 80, 100, 150, 200, 400, 600, 800, 1,000 s/mm². IVIM was performed with a 2D Fourier transform (2DFT) readout to maintain geometric consistency across the optical and MR image sets as opposed to the more common but distortion prone echo-planar imaging. This was done using Bruker's multi-slice spin-echo DWI Standard technique, which is a single spin-echo with diffusion-encoding gradients on either side, and with 2DFT readout for geometrically-robust DWI acquisitions.

E. MRI: Data Analysis

All MRI data was processed using MATLAB (2024b, Mathworks, Natick, MA). IVIM-MRI analysis was performed on voxel-by-voxel basis across the entire dataset. Each voxel was fitted to the biexponential IVIM formula [13]:

$$\frac{S}{S_0} = fe^{-bD_{fast}} + (1-f)e^{-bD_{slow}} \quad (1)$$

where S is the signal intensity, b is the gradient strength, and S_0 is the signal intensity at $b = 0$ s/mm². Solving for all parameters simultaneously has been shown to yield poor fit results [39], so here we used a three-step fitting method. First, (2) was fitted to b-values > 200 s/mm² with a nonlinear least squares regression since in this high b-value regime, D_{fast} contributes negligibly to the signal.

$$S = S_{int}e^{-bD_{slow}} \quad (2)$$

where S_{int} is the $b = 0$ s/mm² intercept for b-values > 200 s/mm². The perfusion fraction, f (Fig. 1G) can then be calculated using (3):

$$f = \frac{S_0 - S_{int}}{S_0} \quad (3)$$

Finally, a partially constrained nonlinear least squares regression was used on (1) to find the value of D_{fast} (Fig. 1H) using D_{slow} and f values just determined. Only voxels with a coefficient of determination, $R^2 > 0.85$ were considered for subsequent analysis.

F. IVIM Monte Carlo Fitting Simulations

A IVIM Monte Carlo fitting simulation was performed to assess the impact of image SNR on IVIM-MRI parameter uncertainty, σ [40]. First the average value of the IVIM parameters were found and the corresponding signal for each b-value was calculated using (1). Gaussian noise was added to the signals corresponding to an SNR range of 5-120. The noisy signal and b-value pairs were then fitted to (1) using the three-step fitting method just described [39] to estimate the IVIM parameters. This process was repeated 100,000 times at each SNR level and the relative error σ for each IVIM parameter x was calculated using (4):

$$\sigma_x = \frac{\sqrt{\frac{1}{N} \sum_{i=1}^N (x_i - x)^2}}{x} \quad (4)$$

where x is the 'true' value of f , D_{fast} , or D_{slow} , x_i is the fitted value of the parameter for the i^{th} trial, and N is the number of simulations (10⁵ here). This provides an estimate of the fitting uncertainties for each IVIM parameter as a function of image SNR.

G. OCT and MRI Correlations

svOCT microvascular maps, DOCT phase shift maps, and IVIM parameter maps were coregistered in 3D using fiducial markers affixed to the window chamber (Fig. 1B) as described in [27]. For MR to optical registration, the fiducial marker registration error [41] was measured to be $164 \pm 57 \mu\text{m}$. Inter-modality spatial correlations were performed using a $1 \times 1 \text{ mm}^2$ lateral by $500 \mu\text{m}$ depth sliding window volume of interest (VOI). The depth of the sliding window VOI corresponded to a single slice from the MRI dataset which matched the OCT analysis depth of $500 \mu\text{m}$ into the tissue. The sliding window VOI was displaced laterally in increments of $500 \mu\text{m}$ to correspond with the size of the MRI voxels. To reduce signal from non-tumour 'healthy' tissue surrounding the tumour, 75% of the sliding window VOI had to be within the tumour contour for the data to be included. For each position of the sliding window VOI, mean values of optical metrics (VVD, $\overline{\Delta\phi}$, fluorescence) were correlated with the corresponding mean values of the IVIM metrics (f , D_{fast} , D_{slow}).

In our previous work comparing DCE-MRI to co-registered svOCT [26], we explored the use of different sliding window VOI lateral sizes including $0.5 \times 0.5 \text{ mm}^2$, $1 \times 1 \text{ mm}^2$, and $1.5 \times 1.5 \text{ mm}^2$. We found that the microvascular correlations were similar regardless of the lateral VOI size; however, voxel-wise comparisons showed a reduction in the correlation coefficients of the resultant micro-macro comparisons likely due to slight registration uncertainties which were amplified when considering these smaller VOIs [26]. In the current work, we thus used a fixed $1 \times 1 \text{ mm}^2$ VOI – a compromise between using a small VOI to accurately capture intratumour vascular heterogeneity while minimizing registration uncertainties.

H. Statistical Analysis

All statistical analysis was performed in MATLAB R2024b (MathWorks, Inc., Natick, MA, USA). For correlation

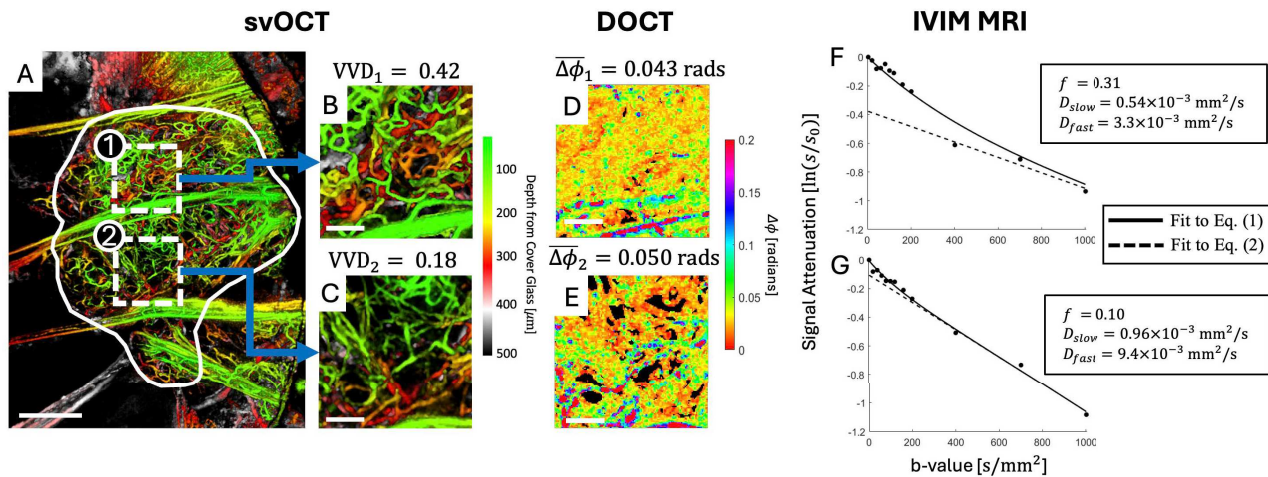


Fig. 2. Optical and IVIM imaging of a representative tumour. (A) Depth encoded svOCT microvascular image with solid white line representing the tumour boundary. Two $1 \times 1 \text{ mm}^2 \times 500 \mu\text{m}$ depth VOI's were chosen for illustrative purposes (dotted white squares). (B) Region 1 has a high VVD. (C) Region 2 has a comparably lower VVD. The Doppler phase shift map for regions 1 and 2 are shown in (D) and (E). (F, G) shows the corresponding IVIM signal attenuation as a function of b for regions 1 and 2. The dotted black lines represent the linear fit to the high b -value data points of (2), and the solid lines represent the full biexponential fit to the data via (1); the quantitative fitting results for the latter are summarized in the solid boxes. (A) scale bar = 1 mm. (B-E) scale bar = $250 \mu\text{m}$.

analysis, IVIM measurements were plotted against the corresponding svOCT microvascular metrics. Linear least squares regression was performed and the Pearson correlation coefficient r was used to assess the strength of the linear relationship. The Pearson correlation coefficient was chosen since it is expected that there is a direct linear relationship between the OCT metrics and IVIM parameters [15]. An r from 0-0.09 was considered a negligible correlation; r from 0.10-0.39 was considered a weak correlation [42]. The p -value was calculated to test the null hypothesis that there is no true correlation between the variables, with $p < 0.05$ being considered statistically significant.

III. RESULTS AND DISCUSSION

Fig. 2A shows a depth encoded svOCT microvascular image of a representative tumour. Two different $1 \times 1 \text{ mm}^2$ (lateral) by $500 \mu\text{m}$ (depth) regions were identified. Region 1 had a high VVD (**Fig. 2B**), and low $\overline{\Delta\phi}$ (**Fig. 2D**). Region 2 had a low VVD (**Fig. 2C**), and high $\overline{\Delta\phi}$ (**Fig. 2E**). The IVIM signal attenuation as a function of b -value for these two regions were plotted (region 1: **Fig. 2F**; region 2: **Fig. 2G**) for direct comparison. The dotted line in **Fig. 2FG** is the fit of (2) to b -values $> 200 \text{ s/mm}^2$. The slope of this line is D_{slow} . Comparing the y -intercept of this line (S_{int}) to the $b = 0$ signal intensity (S_0) gives the value of f (3). The solid black line represents the full IVIM biexponential fit to the data (1) from which D_{fast} was derived ($D_{\text{fast}} \sim$ slope of the biexponential fit in the low b -value region).

Region 1 has a higher VVD than region 2, and this is nicely reflected in a higher value of f in region 1. The higher f in region 1 (**Fig. 2F**) manifests as a larger difference between S_{int} and S_0 compared to the low VVD region (**Fig. 2G**).

If D_{fast} is correlated with blood speed, there should be a smaller D_{fast} for region 1 ($\overline{\Delta\phi} = 0.043$, **Fig. 2D**) compared to region 2 ($\overline{\Delta\phi} = 0.050$, **Fig. 2E**). These example IVIM plots indeed demonstrated this positive relationship since region 1

TABLE I
SUMMARY OF FLUORESCENCE, OCT, AND IVIM INTRA- AND INTER-MODALITY CORRELATIONS

| | | IVIM-MRI | | | OCT | | Fluor. |
|----------|-------------------------|------------------------|-------------------|-------------------|-----------------------|-------------------------|--------|
| | | f | D_{fast} | D_{slow} | VVD | $\overline{\Delta\phi}$ | |
| IVIM-MRI | f | 1 | | | | | |
| | D_{fast} | 0.00 (0.97) | 1 | | | | |
| | D_{slow} | -0.44 (<0.0001) | 0.15 (0.01) | 1 | | | |
| OCT | VVD | 0.34 (<0.0001) | 0.08 (0.18) | -0.04 (0.53) | 1 | | |
| | $\overline{\Delta\phi}$ | 0.18 (0.003) | 0.00 (0.95) | -0.12 (0.05) | 0.18 (0.002) | 1 | |
| Fluor. | | 0.15 (0.02) | -0.09 (0.15) | 0.05 (0.42) | 0.35 (<0.0001) | -0.21 (0.0004) | 1 |

had $D_{\text{fast}} = 3.3 \times 10^{-3} \text{ mm}^2/\text{s}$ and region 2 had a higher D_{fast} of $9.4 \times 10^{-3} \text{ mm}^2/\text{s}$.

Focusing now on the high b -values ($> 200 \text{ s/mm}^2$), there is a smaller D_{slow} in region 1 (**Fig. 2F**) compared to region 2 (**Fig. 2G**). D_{slow} is considered to be inversely proportional to cellular density [43]. Additionally, increased vascular density in tumours may imply increased cellular density since these cells would be better supplied with oxygen and nutrients to support their growth [43]. Taken together, since region 1 has a higher VVD (and likely higher cellular density) than region 2, it is expected that region 1 has a smaller D_{slow} than region 2.

This representative tumour is useful for visualizing how the structure and function of the microvasculature are reflected in, and impact the IVIM-MRI signal; however, to define a more conclusive linkage between the two modalities, larger mice cohorts must be considered. We thus present the intermodality correlation results of our entire 9-mouse dataset in **Table I**, showing both *intramodality* (optical vs. optical metrics and IVIM vs. IVIM metrics) and the more interesting

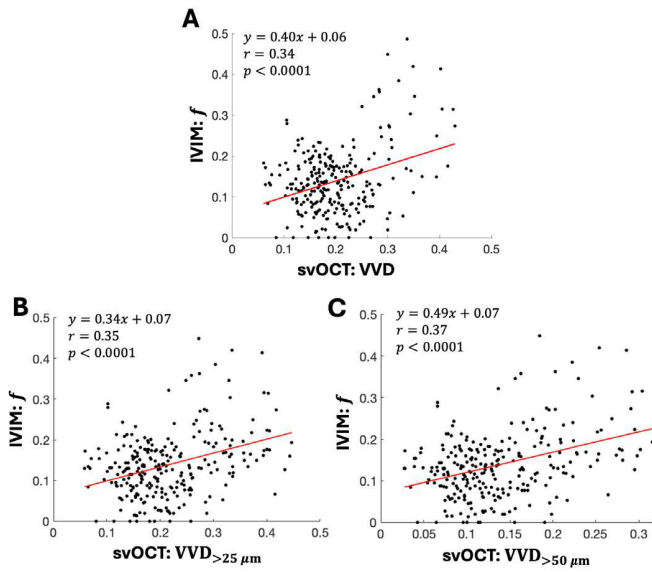


Fig. 3. IVIM's f vs. svOCT's VVD for different vessel diameters. Each point in the plots represents the average value of the given metric for one position of the sliding window VOI. (A) correlation of f with the VVD for all vessels in the tumour. (B,C) correlation of f with the VVD of vessels with diameter $> 25\mu\text{m}$ and $> 50\mu\text{m}$ respectively. The linear least squares fit to the data is shown by the solid red line with the equation of this line, the Pearson correlation coefficient, and p -value shown in each panel. ~ 300 points on each plot represent the data for all $n = 9$ mice (20 - 50 data points/mouse depending on tumour size).

and important intermodality correlations (optical vs. IVIM, red box in Table I) to summarize the complex relationships between parameters. Each entry in Table I lists the Pearson correlation coefficient r between the two variables, with the p -value in brackets. Statistically significant correlations are highlighted in yellow ($p < 0.05$). Note that f was significantly correlated with all optical metrics, D_{slow} was on the verge of being significantly correlated with $\Delta\phi$, and D_{fast} did not show any inter-modality significance.

Focusing on the important intermodality correlations first (red box in Table I), there is a weak positive correlation between VVD and f ($r = 0.34$, $p < 0.0001$, Fig. 3A). This positive relationship is expected according to IVIM theory [13], [15]. To determine if IVIM may be more sensitive to larger vessels, we further subdivided the overall VVD metric into vessel bins with diameters $> 25\mu\text{m}$ ($\text{VVD}_{>25\mu\text{m}}$) and $> 50\mu\text{m}$ ($\text{VVD}_{>50\mu\text{m}}$). The correlation of f with $\text{VVD}_{>25\mu\text{m}}$ is shown in Fig. 3B ($r = 0.35$, $p < 0.0001$) and with $\text{VVD}_{>50\mu\text{m}}$ in Fig. 3C ($r = 0.37$, $p < 0.0001$). There was a slight improvement of the correlation coefficient as the vessel diameter threshold increased ($r = 0.35$ for all vessels, to $r = 0.37$ for vessels with diameter $> 50\mu\text{m}$), indicating that perhaps IVIM-MRI may be more sensitive to larger diameter vessels. But this effect was not large. Overall though, the determined linkage between the underlying VVD and IVIM's f metric provides evidence of the interesting and microvasculature-relevant information content of the latter.

A recent review of histological correlations of vascular density with f found correlation coefficients in the range of ~ 0.4 – 0.9 [23], so our findings are on the lower end of this range. However, this is not a direct comparison since here we are using 3D *in-vivo* svOCT whereas [23] considered 2D *ex-vivo*

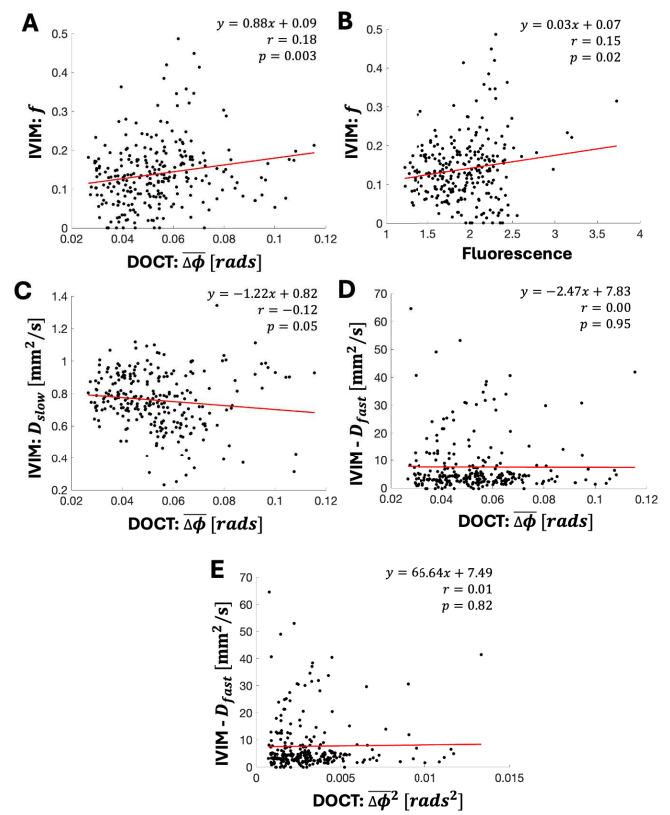


Fig. 4. Additional notable intermodality spatial correlation plots. Each point in the plots represents the average value of the given metric for one position of the sliding window VOI. The linear least squares fit to the data is shown by the solid red line, with its best-fit equation, the Pearson correlation coefficient, and p -value shown in each panel. ~ 300 points on each plot represent the data for all $n = 9$ mice (20-50 data points/mouse depending on tumour size).

histology. The weak correlation found here may suggest that perhaps IVIM has limited microvascular quantification ability; other possible reasons include slight misregistration's between the modalities, IVIM biexponential fitting uncertainties [39], and/or low SNR of MR images [40]. In our previous work we assessed DCE-MRI vs. svOCT correlations and found generally higher correlation coefficients for several DCE-MRI parameters compared to the VVD. For example, DCE-MR's time to peak contrast enhancement with VVD had a correlation coefficient of 0.83 [26]. These results suggest that the benefits of using contrast-agent-free IVIM imaging must be weighed carefully against its potentially reduced ability to quantify tissue microvasculature compared to contrast-enhanced DCE-MRI.

Other notable intermodality correlations from Table I are displayed graphically in Fig. 4A-C. A statistically significant correlation between f and $\Delta\phi$ ($p = 0.003$) was identified, albeit the linear dependence was weak ($r = 0.18$) (Fig. 4A). This relationship may be explained by the presence of large diameter vessels in regions with high f . Larger vessels have been shown to have considerably higher flow speeds compared to small vessels [30], thus reflected in a larger $\Delta\phi$. And the measured f value may be enhanced by larger diameter vessels because either large vessels are more easily detected by IVIM (Fig. 3), or the true perfusion fraction is more sensitive to the presence of large vessels. For example, large vessels

may contribute more to the true perfusion fraction since they occupy more volume than smaller vessels and flow more blood. These conjectures can be corroborated by examining our optical dataset metrics (intra-modality comparisons). There was indeed a significant positive correlation between VVD and $\overline{\Delta\phi}$ ($r = 0.18$, $p = 0.002$, Table I) and a significant positive correlation between VVD and vessel diameter ($r = 0.19$, $p = 0.001$; data not shown). Therefore, the correlation between f and $\overline{\Delta\phi}$ (and similarly VVD and $\overline{\Delta\phi}$) may be due to the presence of larger diameter vessels in high VVD regions.

A statistically significant correlation between f and fluorescence ($p = 0.02$) was also identified, however the linear dependence was again weak ($r = 0.15$) (Fig. 4B). Given that fluorescence is related to viable cellular density [31], [38], increasing perfusion fraction will lead to more oxygen and nutrient supply to the surrounding tumour cells promoting an increase in cellular density [44]. This is further confirmed by referring to the complimentary optical metrics, as there is a positive correlation between VVD and fluorescence ($r = 0.35$, $p < 0.0001$, Table I). Another way to examine the positive relationship between f and fluorescence is to consider the intra-modality correlation between f and D_{slow} ($r = -0.44$, $p < 0.0001$, Table I). D_{slow} has been shown to be inversely proportional to cellular density [43], thus increasing f should lead to increased cellular density and a corresponding decrease in D_{slow} as seen in our results. However, this relationship must be interpreted cautiously since there was no correlation identified between D_{slow} and fluorescence ($r = 0.05$, $p = 0.42$, Table I). One possible explanation for the lack of correlation between D_{slow} and fluorescence is that the maturation of DsRed protein is slow *in-vivo*, with a half-life of 1 day [45] suggesting that the cellular density may not be directly related to the measured fluorescence signal. Alternatively, there may not be enough dynamic range in cellular density amongst these tumours to pick up an appreciable signal difference in D_{slow} .

Interestingly, $\overline{\Delta\phi}$ vs. D_{slow} was on the verge of being statistically significant ($r = -0.12$, $p = 0.05$, Fig. 4C). Keeping in mind that D_{slow} is inversely proportional to cellular density [43], this relationship may be caused by blood vessel compression and/or increased interstitial fluid pressure in these high cellular density regions that may restrict flow [46]. This is consistent the observed significant negative intramodality correlation between $\overline{\Delta\phi}$ and fluorescence ($r = -0.21$, $p = 0.0004$) (Table I). Again, this relationship must be interpreted carefully considering the lack of correlation between fluorescence and D_{slow} .

Surprisingly, IVIM's D_{fast} metric did not correlate with any ground-truth optical measurements. For example, there was no correlation identified between $\overline{\Delta\phi}$ and D_{fast} ($r = 0.00$, $p = 0.95$, Fig. 4D) despite the proposed theoretical relationship of $D_{fast} = \bar{v}/6$ [15]. However, this model assumes a tissue milieu in which the blood flow changes directions rapidly between gradient pulses, mimicking a random diffusion process. Here, the blood is assumed to change direction after traversing a single vessel segment, so the blood must be travelling sufficiently fast to traverse several vessel segments (and thus change direction) between gradient pulses. In this work, the average vessel segment length was measured to be $77 \pm 7 \mu\text{m}$ (mean \pm standard deviation). The average blood speed was

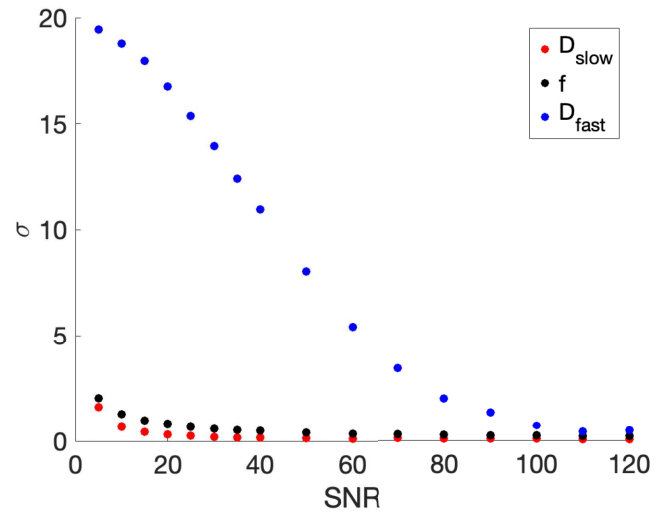


Fig. 5. Monte Carlo simulation to assess IVIM parameter uncertainties. The relative error σ is shown for each fitted IVIM parameter as a function of SNR. Each SNR value was fit 100,000 times.

calculated by accounting for the Doppler angle of each vessel segment as described in [30], yielding $\bar{v} = 0.66 \pm 0.24$ mm/s. The time between gradient pulses Δ was 9 ms; thus an average red blood cell moves only $\sim 6 \mu\text{m}$ in this time, which is much shorter than the average vessel segment length, indicating that this diffusion-like relationship may not hold in these tumours.

Le Bihan further proposed the quadratic dependence on average velocity via $D_{fast} = \bar{v}^2\Delta/6$ where Δ is the gradient pulse separation time [15], [47]. This equation is valid when blood is flowing slow enough that it will remain in one vessel segment during the time Δ and when the gradient duration δ is much smaller than Δ . This quadratic relationship may be more appropriate for our case due to the low blood speeds. Thus, in accord with this low-speed model, we would expect $D_{fast} \propto \overline{\Delta\phi}^2$ (assuming that $\overline{\Delta\phi} \propto \bar{v}$). Fig. 4E shows D_{fast} vs. $\overline{\Delta\phi}^2$ plot, yet disappointingly there was still no correlation, indicating the inability of D_{fast} to accurately report on blood speed. However, this also may be an inappropriate comparison since the relationship $D_{fast} = \bar{v}^2\Delta/6$ is only valid when $\delta \ll \Delta$, which is only partially the case in this experiment ($\delta = 2.2$ ms, $\Delta = 9$ ms). Increasing the time between gradient pulses might improve these correlations.

To separate the perfusion and diffusion components in the MR signal, and ultimately accurately measure f , D_{fast} must be considerably higher than D_{slow} [15]. Therefore, it is quite surprising that a robust correlation was found between VVD and f (Fig. 3) but not between $\overline{\Delta\phi}$ and D_{fast} (Fig. 4D-E). To make sense of this consider that while D_{fast} has been accurately measured in phantom studies [48], in real *in-vivo* tissue its determination has proven to be much more difficult [40], [49]. Studies have indicated that precise estimation of D_{fast} demands very high SNR, whereas f can be measured well at comparably lower SNR [40], [49], [50]. To quantify the uncertainties associated with fitting each of the IVIM parameters in this experiment, the predictions of a Monte Carlo fitting simulation are shown in Fig. 5, where the average values of the IVIM parameters from our dataset were used ($f = 0.14$, $D_{slow} = 0.74$ mm²/s, and $D_{fast} = 7.79$ mm²/s).

The range of SNRs across all fitted voxels in this study was measured to be 8–31; from Fig. 5, this suggests that D_{fast} had approximately 10–25 times more error in its determined value compared to f . An SNR value of 120 was required to achieve a relative error in D_{fast} of <50%. Therefore, given the relatively modest correlation dependence between VVD and the fairly-accurately-determined f ($r = 0.34$, Fig. 3A), it is perhaps not surprising that in the presence of much larger uncertainty in D_{fast} , there were no correlations identified between it and $\Delta\phi$ (nor with any other optical ground-truth microvascular metric).

IV. STUDY LIMITATIONS AND FUTURE WORK

Our IVIM Monte Carlo fitting simulation results indicated that the lack of correlation between D_{fast} and $\Delta\phi$ was likely due to SNR limitations of IVIM, specifically in its uncertainty for D_{fast} estimation (Fig. 5). The modest tissue thickness and complex geometry of the DSWC made it challenging to achieve high SNR images for several reasons. First, in the absence of a local RF receiver coil integrated into the DSWC, a larger (86 mm) diameter RF coil was required to accommodate the scan bed, mouse, and window chamber. This design inherently reduces the SNR. Second, a practical limitation of the scan time to a one-hour acquisition prevented SNR improvements by data averaging or imaging parameter modification. This long scan time was required to implement multi-b-value DWI with a 2DFT readout, rather than with echo-planar imaging. A 2DFT readout was required to spatially resolve the tumour and reduce distortions for accurate optical to MR coregistration. For future *preclinical* work, it is suggested that a local receive coil be designed for the window chamber to improve the SNR [51].

From these findings and those of others [40], [49], [50], it seems infeasible to achieve accurate measurements of D_{fast} *in-vivo* preclinically or in the clinic due to SNR limitations. Our results do support the use of solely acquiring large b-value images ($> 200 \text{ s/mm}^2$) to calculate f and D_{slow} . This protocol modification would significantly reduce the imaging time requirements, making it more useable in a busy clinical setting. Many groups have already resorted to this methodology [52], [53]. In the context of cancer radiotherapy, measuring f may enable detection of potentially hypoxic regions which could enable treatment personalization via dose painting [6] or fractionation adjustments [7]. f may also prove to be an important parameter for longitudinally quantifying the effects of vascular targeting agents, which could help inform clinicians on the optimal timing of adjuvant therapies [9]. More advanced MR imaging methods may be needed to increase the SNR to accurately measure D_{fast} . These include using higher field strength MR systems, more sensitive radiofrequency coils, or perhaps AI-based denoising methods [54].

Aside from SNR limitations, the IVIM signal may be better modeled by considering two vascular pools: capillaries with slow flow and larger vessels with faster flow as described by Fournet et al. [55]. This model includes measurements of D_{fast} and f for each of the flow compartments (thus two D_{fast} and two f determinations) [56]. While this may be a more suitable description of the IVIM signal (potentially

leading to improved D_{fast} microvascular correlations), the robustness and suitability of data fitting using a 4-parameter model must be carefully evaluated. Tensor IVIM evaluation is also an important future research direction given that the IVIM signal may be directionally dependent [57]; however, this was not explored due to animal welfare considerations during the already long (61 minutes) 3-gradient direction acquisition used here.

The 3D imaging capabilities of svOCT provide a useful preclinical platform to study other assumptions of the IVIM model, for example that capillaries are randomly orientated in 3D. To test this, the vessels may be skeletonized and the orientation distribution function [58] could be used to determine the degree of randomness and possible anisotropy. Future work could seek to identify how different vessel orientations impact the IVIM signal and resultant micro-macro correlations.

For high-resolution optical imaging with OCT, capillary velocimetry still remains challenging. The low velocities and low backscattered signal arising from individual red blood cells in capillaries restrict the detection limits of DOCT. The angle dependence of the Doppler effect is another limitation, with signal disappearance (to first order) in perpendicular-to-the-imaging-beam flow direction. The colour Doppler method presented here thus represents the average axial component of the velocity vector, and the true 3D nature of the tumour microvascular geometry and flow, even if corrected *a posteriori*, can still introduce uncertainty [30]. Since D_{fast} is sensitive to blood flow in all directions, its comparison with only the average *axial* component of the blood speed ($\Delta\phi$), as reported by doppler OCT, may help explain the lack of correlation here.

We chose a pancreatic adenocarcinoma cell line because it presents a highly heterogenous tumour microvascular network [59] potentially representative of a broad range of cancers. This vascular heterogeneity is demonstrated in the wide range of measured VVD values ranging from 0.05 to 0.5 (Fig. 3A). The results presented here indicate that IVIM's f is able to differentiate between this wide range of VVD values which is promising for its use in various tumour sites that have different levels of vascularity. But generalizability of the findings must await more studies with different tumour types and anatomic locations. In practical terms, the DSWC model is very advantageous since bulk tissue motion is minimized as the tumour is away from the mouse body and can be fixed to the MR bed/imaging stage [27]. However, motion artifacts will be an important consideration for other practical imaging arrangements. For example, future studies should explore the adaptation of this intermodality registration protocol to more biologically realistic scenarios such as the orthotopic abdominal window chamber model [60].

Studies have investigated using IVIM-MRI to longitudinally monitor the tumour microvascular network to treatments by comparing with histology [61] and other perfusion MRI methods [62]. The plastic DSWC design explored here provides a useful methodology to accurately perform longitudinal svOCT-validated IVIM-MRI, for example in monitoring the response of normal and pathologic tissues to different vascular targeting treatments [27].

V. CONCLUSION

To our knowledge, this is the first direct *in-vivo* quantitative spatial comparison between IVIM-MRI and high-resolution 3D optical imaging. Significant positive correlations were noted between VVD (measured with svOCT) and f (measured with IVIM-MRI); this MR perfusion metric also correlated with several other optically-measured variables. These correlations strengthen the case for using IVIM-MRI in the clinic to quantify tissue microvasculature by linking its metrics to underlying microvascular properties. However, if one is willing to use contrast agents, contrast enhanced perfusion MR methods likely offer more accurate measurements and stronger linkages to underlying microvascular properties [26]. If using contrast enhanced MRI, one should consider patient contraindications for contrast [11], the risk of Gadolinium deposition [11], and potential reproducibility uncertainties [12]. IVIM's D_{fast} was not correlated with any optically-reported measure of blood microvasculature; corresponding Monte Carlo simulations highlighted the requirement for high SNR images for accurate D_{fast} determination. These findings suggest that acquiring high b-value images to measure f only is the likely practical approach, with the added benefit of reducing patient scan time. Overall, these direct comparisons of IVIM metrics with the underlying 3D microvascular parameters determined with OCT provide useful ground-truth interpretations of MR perfusion measurements.

REFERENCES

- [1] B. Muz, P. de la Puente, F. Azab, and A. K. Azab, "The role of hypoxia in cancer progression, angiogenesis, metastasis, and resistance to therapy," *Hypoxia*, vol. 3, pp. 83–92, Dec. 2015, doi: [10.2147/hp.s93413](https://doi.org/10.2147/hp.s93413).
- [2] R. K. Jain, "The next frontier of molecular medicine: Delivery of therapeutics," *Nature Med.*, vol. 4, no. 6, pp. 655–657, Jun. 1998, doi: [10.1038/nm0698-655](https://doi.org/10.1038/nm0698-655).
- [3] C. Viillard and B. Larrivée, "Tumor angiogenesis and vascular normalization: Alternative therapeutic targets," *Angiogenesis*, vol. 20, no. 4, pp. 409–426, Nov. 2017, doi: [10.1007/s10456-017-9562-9](https://doi.org/10.1007/s10456-017-9562-9).
- [4] W. Li, Y.-Y. Quan, Y. Li, L. Lu, and M. Cui, "Monitoring of tumor vascular normalization: The key points from basic research to clinical application," *Cancer Manage. Res.*, vol. 10, pp. 4163–4172, Oct. 2018, doi: [10.2147/cmar.s174712](https://doi.org/10.2147/cmar.s174712).
- [5] S. V. Kozin, "Vascular damage in tumors: A key player in stereotactic radiation therapy?," *Trends Cancer*, vol. 8, no. 10, pp. 806–819, Oct. 2022, doi: [10.1016/j.trecan.2022.06.002](https://doi.org/10.1016/j.trecan.2022.06.002).
- [6] S. M. Bentzen and V. Gregoire, "Molecular imaging-based dose painting: A novel paradigm for radiation therapy prescription," *Seminars Radiat. Oncol.*, vol. 21, no. 2, pp. 101–110, Apr. 2011, doi: [10.1016/j.semradonc.2010.10.001](https://doi.org/10.1016/j.semradonc.2010.10.001).
- [7] J. Jeong, K. I. Shoghi, and J. O. Deasy, "Modelling the interplay between hypoxia and proliferation in radiotherapy tumour response," *Phys. Med. Biol.*, vol. 58, no. 14, pp. 4897–4919, Jul. 2013, doi: [10.1088/0031-9155/58/14/4897](https://doi.org/10.1088/0031-9155/58/14/4897).
- [8] G. Brix, J. Griebel, F. Kiessling, and F. Wenz, "Tracer kinetic modelling of tumour angiogenesis based on dynamic contrast-enhanced CT and MRI measurements," *Eur. J. Nucl. Med. Mol. Imag.*, vol. 37, no. S1, pp. 30–51, Aug. 2010, doi: [10.1007/s00259-010-1448-7](https://doi.org/10.1007/s00259-010-1448-7).
- [9] J. Yang et al., "MR imaging biomarkers evaluating vascular normalization window after anti-vessel treatment," *Oncotarget*, vol. 9, no. 15, pp. 11964–11976, Feb. 2018, doi: [10.18632/oncotarget.22600](https://doi.org/10.18632/oncotarget.22600).
- [10] A. Shukla-Dave et al., "Dynamic contrast-enhanced magnetic resonance imaging as a predictor of outcome in head-and-neck squamous cell carcinoma patients with nodal metastases," *Int. J. Radiat. Oncol. Biol. Phys.*, vol. 82, no. 5, pp. 1837–1844, Apr. 2012, doi: [10.1016/j.ijrobp.2011.03.006](https://doi.org/10.1016/j.ijrobp.2011.03.006).
- [11] K. M. Hasebroock and N. J. Serkova, "Toxicity of MRI and CT contrast agents," *Expert Opinion Drug Metabolism Toxicology*, vol. 5, no. 4, pp. 403–416, Apr. 2009, doi: [10.1517/17425250902873796](https://doi.org/10.1517/17425250902873796).
- [12] T. Heye et al., "Reproducibility of dynamic contrast-enhanced MR imaging. Part I. Perfusion characteristics in the female pelvis by using multiple computer-aided diagnosis perfusion analysis solutions," *Radiology*, vol. 266, no. 3, pp. 801–811, Mar. 2013, doi: [10.1148/radiol.12120278](https://doi.org/10.1148/radiol.12120278).
- [13] D. Le Bihan, E. Breton, D. Lallemand, M. L. Aubin, J. Vignaud, and M. Laval-Jeantet, "Separation of diffusion and perfusion in intravoxel incoherent motion MR imaging," *Radiology*, vol. 168, no. 2, pp. 497–505, Aug. 1988, doi: [10.1148/radiology.168.2.3393671](https://doi.org/10.1148/radiology.168.2.3393671).
- [14] M. Iima and D. Le Bihan, "Clinical intravoxel incoherent motion and diffusion MR imaging: Past, present, and future," *Radiology*, vol. 278, no. 1, pp. 13–32, Jan. 2016, doi: [10.1148/radiol.2015150244](https://doi.org/10.1148/radiol.2015150244).
- [15] D. Le Bihan, "What can we see with IVIM MRI?," *NeuroImage*, vol. 187, pp. 56–67, Feb. 2019, doi: [10.1016/j.neuroimage.2017.12.062](https://doi.org/10.1016/j.neuroimage.2017.12.062).
- [16] H. J. Lee et al., "Tumor perfusion-related parameter of diffusion-weighted magnetic resonance imaging: Correlation with histological microvessel density," *Magn. Reson. Med.*, vol. 71, no. 4, pp. 1554–1558, 2014, doi: [10.1002/mrm.24810](https://doi.org/10.1002/mrm.24810).
- [17] A. Surov et al., "Correlations between intravoxel incoherent motion (IVIM) parameters and histological findings in rectal cancer: Preliminary results," *Oncotarget*, vol. 8, no. 13, pp. 21974–21983, Mar. 2017, doi: [10.18632/oncotarget.15753](https://doi.org/10.18632/oncotarget.15753).
- [18] H. Chandarana et al., "Diffusion-weighted intravoxel incoherent motion imaging of renal tumors with histopathologic correlation," *Investigative Radiol.*, vol. 47, no. 12, pp. 688–696, Dec. 2012, doi: [10.1097/rli.0b013e31826a0a49](https://doi.org/10.1097/rli.0b013e31826a0a49).
- [19] C. Liu et al., "Intravoxel incoherent motion MR imaging for breast lesions: Comparison and correlation with pharmacokinetic evaluation from dynamic contrast-enhanced MR imaging," *Eur. Radiol.*, vol. 26, no. 11, pp. 3888–3898, Nov. 2016, doi: [10.1007/s00330-016-4241-6](https://doi.org/10.1007/s00330-016-4241-6).
- [20] S. Marzi, L. Stefanetti, F. Sperati, and V. Anelli, "Relationship between diffusion parameters derived from intravoxel incoherent motion MRI and perfusion measured by dynamic contrast-enhanced MRI of soft tissue tumors," *NMR Biomed.*, vol. 29, no. 1, pp. 6–14, Jan. 2016, doi: [10.1002/nbm.3446](https://doi.org/10.1002/nbm.3446).
- [21] S. Bisdas et al., "Correlative assessment of tumor microcirculation using contrast-enhanced perfusion MRI and intravoxel incoherent motion diffusion-weighted MRI: Is there a link between them?," *NMR Biomed.*, vol. 27, no. 10, pp. 1184–1191, 2014, doi: [10.1002/nbm.3172](https://doi.org/10.1002/nbm.3172).
- [22] D. M. McDonald and P. L. Choyke, "Imaging of angiogenesis: From microscope to clinic," *Nature Med.*, vol. 9, no. 6, pp. 713–725, Jun. 2003, doi: [10.1038/nm0603-713](https://doi.org/10.1038/nm0603-713).
- [23] C. Federau, "Intravoxel incoherent motion MRI as a means to measure in vivo perfusion: A review of the evidence," *NMR Biomed.*, vol. 30, no. 11, p. e3780, Nov. 2017, doi: [10.1002/nbm.3780](https://doi.org/10.1002/nbm.3780).
- [24] J.-V. Gaustad, K. G. Brurberg, T. G. Simonsen, C. S. Mollatt, and E. K. Rofstad, "Tumor vascularity assessed by magnetic resonance imaging and intravital microscopy imaging," *Neoplasia*, vol. 10, no. 4, pp. 354–362, Apr. 2008, doi: [10.1593/neo.08162](https://doi.org/10.1593/neo.08162).
- [25] N. K. Reitan, M. Thuen, P. E. Goa, and C. de Lange Davies, "Characterization of tumor microvascular structure and permeability: Comparison between magnetic resonance imaging and intravital confocal imaging," *J. Biomed. Opt.*, vol. 15, no. 3, 2010, Art. no. 036004, doi: [10.1117/1.3431095](https://doi.org/10.1117/1.3431095).
- [26] W. J. Zabel, N. Allam, W. D. Foltz, C. Fluerau, E. Taylor, and I. A. Vitkin, "Bridging the macro to micro resolution gap with angiographic optical coherence tomography and dynamic contrast enhanced MRI," *Sci. Rep.*, vol. 12, no. 1, p. 3159, Feb. 2022, doi: [10.1038/s41598-022-07000-1](https://doi.org/10.1038/s41598-022-07000-1).
- [27] W. J. Zabel et al., "A dorsal skinfold window chamber tumor mouse model for combined intravital microscopy and magnetic resonance imaging in translational cancer research," *J. Vis. Exp.*, no. 206, 2024, Art. no. e66383, doi: [10.3791/66383](https://doi.org/10.3791/66383).
- [28] A. Mariampillai et al., "Speckle variance detection of microvasculature using swept-source optical coherence tomography," *Opt. Lett.*, vol. 33, no. 13, pp. 1530–1532, Jul. 2008, doi: [10.1364/ol.33.001530](https://doi.org/10.1364/ol.33.001530).
- [29] A. Mariampillai et al., "Optimized speckle variance OCT imaging of microvasculature," *Opt. Lett.*, vol. 35, no. 8, pp. 1257–1259, Apr. 2010, doi: [10.1364/ol.35.001257](https://doi.org/10.1364/ol.35.001257).
- [30] H. A. Contreras-Sánchez, W. J. Zabel, C. Fluerau, L. Lilge, E. Taylor, and A. Vitkin, "Characterizing normal and tumour blood microcirculatory systems using optical coherence tomography," *Photonics*, vol. 11, no. 9, p. 891, Sep. 2024, doi: [10.3390/photonics11090891](https://doi.org/10.3390/photonics11090891).

- [31] M. H. Tan et al., "Characterization of a new primary human pancreatic tumor line," *Cancer Invest.*, vol. 4, no. 1, pp. 15–23, Jan. 1986, doi: [10.3109/07357908609039823](https://doi.org/10.3109/07357908609039823).
- [32] Y. Mao, S. Sherif, C. Fluerau, and S. Chang, "3×3 Mach-Zehnder interferometer with unbalanced differential detection for full-range swept-source optical coherence tomography," *Appl. Opt.*, vol. 47, no. 12, pp. 2004–2010, Apr. 2008, doi: [10.1364/ao.47.002004](https://doi.org/10.1364/ao.47.002004).
- [33] J. Tang, S. E. Erdener, B. Fu, and D. A. Boas, "Capillary red blood cell velocimetry by phase-resolved optical coherence tomography," *Opt. Lett.*, vol. 42, no. 19, pp. 3976–3979, Oct. 2017, doi: [10.1364/ol.42.003976](https://doi.org/10.1364/ol.42.003976).
- [34] L. Conroy, R. S. DaCosta, and I. A. Vitkin, "Quantifying tissue microvasculature with speckle variance optical coherence tomography," *Opt. Lett.*, vol. 37, no. 15, pp. 3180–3182, Aug. 2012, doi: [10.1364/ol.37.003180](https://doi.org/10.1364/ol.37.003180).
- [35] B. J. Vakoc et al., "Three-dimensional microscopy of the tumor microenvironment in vivo using optical frequency domain imaging," *Nature Med.*, vol. 15, no. 10, pp. 1219–1223, Oct. 2009, doi: [10.1038/nm.1971](https://doi.org/10.1038/nm.1971).
- [36] N. Otsu, "A threshold selection method from gray-level histograms," *IEEE Trans. Syst., Man, Cybern.*, vol. SMC-9, no. 1, pp. 62–66, Jan. 1979, doi: [10.1109/TSMC.1979.4310076](https://doi.org/10.1109/TSMC.1979.4310076).
- [37] J. M. Fitzpatrick and M. Sonka, *Handbook of Medical Imaging, Volume 2: Medical Image Processing and Analysis*. Bellingham, WA, USA: SPIE Press, 2000.
- [38] C. Ricard, F. Stanchi, T. Rodriguez, M.-C. Amoureux, G. Rougon, and F. Debarbieux, "Dynamic quantitative intravital imaging of glioblastoma progression reveals a lack of correlation between tumor growth and blood vessel density," *PLoS ONE*, vol. 8, no. 9, Sep. 2013, Art. no. e72655, doi: [10.1371/journal.pone.0072655](https://doi.org/10.1371/journal.pone.0072655).
- [39] E. K. Englund, D. B. Berry, J. J. Behun, L. R. Frank, S. R. Ward, and B. Shahidi, "Assessment of fitting methods and variability of IVIM parameters in muscles of the lumbar spine at rest," *Frontiers Musculoskeletal Disorders*, vol. 2, Apr. 2024, Art. no. 1386276, doi: [10.3389/fmscd.2024.1386276](https://doi.org/10.3389/fmscd.2024.1386276).
- [40] A. Lemke, B. Stieltjes, L. R. Schad, and F. B. Laun, "Toward an optimal distribution of b values for intravoxel incoherent motion imaging," *Magn. Reson. Imag.*, vol. 29, no. 6, pp. 766–776, Jul. 2011, doi: [10.1016/j.mri.2011.03.004](https://doi.org/10.1016/j.mri.2011.03.004).
- [41] J. B. West, J. M. Fitzpatrick, S. A. Toms, C. R. Maurer, and R. J. Maciunas, "Fiducial point placement and the accuracy of point-based, rigid body registration," *Neurosurgery*, vol. 48, no. 4, pp. 810–817, Apr. 2001, doi: [10.1097/00006123-200104000-00023](https://doi.org/10.1097/00006123-200104000-00023).
- [42] P. Schober, C. Boer, and L. A. Schwarte, "Correlation coefficients: Appropriate use and interpretation," *Anesthesia Analgesia*, vol. 126, no. 5, pp. 1763–1768, May 2018, doi: [10.1213/ane.0000000000002864](https://doi.org/10.1213/ane.0000000000002864).
- [43] L. Chen et al., "The correlation between apparent diffusion coefficient and tumor cellularity in patients: A meta-analysis," *PLoS ONE*, vol. 8, no. 11, Nov. 2013, Art. no. e79008, doi: [10.1371/journal.pone.0079008](https://doi.org/10.1371/journal.pone.0079008).
- [44] K. E. de Visser and J. A. Joyce, "The evolving tumor microenvironment: From cancer initiation to metastatic outgrowth," *Cancer Cell*, vol. 41, no. 3, pp. 374–403, Mar. 2023, doi: [10.1016/j.ccell.2023.02.016](https://doi.org/10.1016/j.ccell.2023.02.016).
- [45] L. A. Gross, G. S. Baird, R. C. Hoffman, K. K. Baldrige, and R. Y. Tsien, "The structure of the chromophore within DsRed, a red fluorescent protein from coral," *Proc. Nat. Acad. Sci. USA*, vol. 97, no. 22, pp. 11990–11995, Oct. 2000, doi: [10.1073/pnas.97.22.11990](https://doi.org/10.1073/pnas.97.22.11990).
- [46] T. P. Padera, B. R. Stoll, J. B. Tooredman, D. Capen, E. D. Tomaso, and R. K. Jain, "Cancer cells compress intratumour vessels," *Nature*, vol. 427, no. 6976, p. 695, Feb. 2004, doi: [10.1038/427695a](https://doi.org/10.1038/427695a).
- [47] D. Le Bihan, "Magnetic resonance imaging of perfusion," *Magn. Reson. Med.*, vol. 14, no. 2, pp. 283–292, May 1990, doi: [10.1002/mrm.1910140213](https://doi.org/10.1002/mrm.1910140213).
- [48] M. J. Schneider, T. Gaass, J. Ricke, J. Dinkel, and O. Dietrich, "Assessment of intravoxel incoherent motion MRI with an artificial capillary network: Analysis of biexponential and phase-distribution models," *Magn. Reson. Med.*, vol. 82, no. 4, pp. 1373–1384, Oct. 2019, doi: [10.1002/mrm.27816](https://doi.org/10.1002/mrm.27816).
- [49] J. A. Vasquez et al., "Reproducibility and repeatability of intravoxel incoherent motion MRI acquisition methods in liver," *J. Magn. Reson. Imag.*, vol. 60, no. 4, pp. 1691–1703, 2024, doi: [10.1002/jmri.29249](https://doi.org/10.1002/jmri.29249).
- [50] S. S. Javidi, A. Shirazinodeh, and H. S. Rad, "Intravoxel incoherent motion quantification dependent on measurement SNR and tissue perfusion: A simulation study," *J. Biomed. Phys. Eng.*, vol. 13, no. 6, pp. 555–562, 2023, doi: [10.31661/jbpe.v0i0.2102-1281](https://doi.org/10.31661/jbpe.v0i0.2102-1281).
- [51] H. M. Leung, R. Schafer, M. M. Pagel, I. F. Robey, and A. F. Gmitro, "Multimodality pH imaging in a mouse dorsal skin fold window chamber model," *Proc. SPIE*, vol. 2, no. 8574, 2013, Art. no. 85740L, doi: [10.1117/12.2005472](https://doi.org/10.1117/12.2005472).
- [52] Q. Yuan et al., "Quantitative diffusion-weighted imaging and dynamic contrast-enhanced characterization of the index lesion with multiparametric MRI in prostate cancer patients," *J. Magn. Reson. Imag.*, vol. 45, no. 3, pp. 908–916, Mar. 2017, doi: [10.1002/jmri.25391](https://doi.org/10.1002/jmri.25391).
- [53] O. Jalnefjord et al., "Comparison of methods for estimation of the intravoxel incoherent motion (IVIM) diffusion coefficient (D) and perfusion fraction (f)," *Magn. Reson. Mater. Phys., Biol. Med.*, vol. 31, no. 6, pp. 715–723, Dec. 2018, doi: [10.1007/s10334-018-0697-5](https://doi.org/10.1007/s10334-018-0697-5).
- [54] H. Chung, E. S. Lee, and J. C. Ye, "MR image denoising and super-resolution using regularized reverse diffusion," *IEEE Trans. Med. Imag.*, vol. 42, no. 4, pp. 922–934, Apr. 2023, doi: [10.1109/TMI.2022.3220681](https://doi.org/10.1109/TMI.2022.3220681).
- [55] G. Fournet, J.-R. Li, A. M. Cerjanic, B. P. Sutton, L. Ciobanu, and D. Le Bihan, "A two-pool model to describe the IVIM cerebral perfusion," *J. Cerebral Blood Flow Metabolism*, vol. 37, no. 8, pp. 2987–3000, Aug. 2017, doi: [10.1177/0271678x16681310](https://doi.org/10.1177/0271678x16681310).
- [56] A. Maiuro et al., "Two-compartment perfusion MR IVIM model to investigate normal and pathological placental tissue," *J. Magn. Reson. Imag.*, vol. 59, no. 3, pp. 879–891, Mar. 2024, doi: [10.1002/jmri.28858](https://doi.org/10.1002/jmri.28858).
- [57] T. Finkenstaedt et al., "The IVIM signal in the healthy cerebral gray matter: A play of spherical and non-spherical components," *NeuroImage*, vol. 152, pp. 340–347, May 2017, doi: [10.1016/j.neuroimage.2017.03.004](https://doi.org/10.1016/j.neuroimage.2017.03.004).
- [58] U. F. Kocks, C. N. Tomé, and H. R. Wenk, *Texture and Anisotropy*. Cambridge, U.K.: Cambridge Univ. Press, 2001.
- [59] C. Metran-Nascente et al., "Measurement of tumor hypoxia in patients with advanced pancreatic cancer based on ¹⁸F-fluoroazomyin arabinoside uptake," *J. Nucl. Med.*, vol. 57, no. 3, pp. 361–366, Mar. 2016, doi: [10.2967/jnumed.115.167650](https://doi.org/10.2967/jnumed.115.167650).
- [60] T. Samuel, S. Ropic, C. O'Brien, M. Edson, Y. Zhong, and R. S. DaCosta, "Quantitative intravital imaging for real-time monitoring of pancreatic tumor cell hypoxia and stroma in an orthotopic mouse model," *Sci. Adv.*, vol. 9, no. 23, Jun. 2023, Art. no. eade8672, doi: [10.1126/sciadv.ade8672](https://doi.org/10.1126/sciadv.ade8672).
- [61] J. Liang et al., "Application of IVIM-DWI in detecting the tumor vasculogenic mimicry under antiangiogenesis combined with oxaliplatin treatment," *Frontiers Oncol.*, vol. 10, p. 1376, Aug. 2020, doi: [10.3389/fonc.2020.01376](https://doi.org/10.3389/fonc.2020.01376).
- [62] E. S. Kooreman, V. van Pelt, M. E. Nowee, F. Pos, U. A. van der Heide, and P. J. van Houdt, "Longitudinal correlations between intravoxel incoherent motion (IVIM) and dynamic contrast-enhanced (DCE) MRI during radiotherapy in prostate cancer patients," *Frontiers Oncol.*, vol. 12, Jun. 2022, Art. no. 897130, doi: [10.3389/fonc.2022.897130](https://doi.org/10.3389/fonc.2022.897130).